ACS APPLIED MATERIALS & INTERFACES

Research Article

www.acsami.org

Aggregation-Induced Near-Infrared Absorption of Squaraine Dye in an Albumin Nanocomplex for Photoacoustic Tomography in Vivo

Fei-Fei An,[†,‡] Zi-Jian Deng,[‡,§] Jun Ye,[†] Jin-Feng Zhang,[†] Yin-Long Yang,[⊥] Chang-Hui Li,[*,§] Cai-Jun Zheng,[†] and Xiao-Hong Zhang[*,†,⊥]

[†]Nano-organic Photoelectronic Laboratory and Key Laboratory of Photochemical Conversion and Optoelectronic Materials, Technical Institute of Physics and Chemistry, Chinese Academy of Sciences, Beijing 100190, P. R. China

[§]Department of Biomedical Engineering, College of Engineering, Peking University, Beijing 100871, China

[⊥]Functional Nano & Soft Materials Laboratory (FUNSOM), Jiangsu Key Laboratory for Carbon-Based Functional Materials & Devices and Collaborative Innovation Center of Suzhou Nano Science and Technology, Soochow University, Suzhou, Jiangsu 215123, P. R. China

Supporting Information

ABSTRACT: Photoacoustic tomography (PAT) is a newly emerging noninvasive imaging modality that could be further enhanced using near-infrared (NIR)-absorbing materials as contrast agents. To date, the most extensively studied photoacoustic imaging agents are inorganic nanomaterials because organic materials with NIR-absorption capabilities are limited. In this study, a NIR-absorbing nanocomplex composed of a squaraine dye (SQ) and albumin was prepared based on the aggregation-induced NIR absorption of SQ. Through aggregation, the absorption spectrum of SQ was widened from the visible-light region to the NIR region, which facilitated photoacoustic signal generation in the tissue-transparent NIR optical window (700–900 nm). Blood analysis and histology measurements revealed that the nanocomplex can be used for PAT applications in vivo without obvious toxicity to living mice.

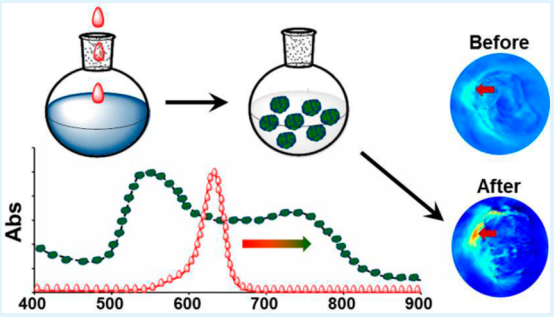

KEYWORDS: *albumin, squaraine dye, nanocomplex, photoacoustic tomography, near-infrared, red shift*

INTRODUCTION

Photoacoustic tomography (PAT) is a newly emerging noninvasive imaging modality with higher resolution and significantly greater penetration depth than other optical imaging techniques.[1] This technique involves the local absorption of pulsed laser light by tissues, which results in transient thermoelastic expansion. The generation of pressure waves can then be detected with an ultrasound transducer. Biological tissues are well-known to absorb light weakly in the tissue-transparent near-infrared (NIR) optical window (700–900 nm).[2] For excitation light to achieve deeper tissue penetration, a pulse laser with NIR-region wavelength needs to be utilized. However, disease sites are also transparent to NIR light and insensitive to PAT. To address this problem, several nanomaterials with strong NIR-region absorbance have been explored as exogenous photoacoustic contrast agents for in vivo imaging and diagnosis.[3] To date, the most extensively studied photoacoustic imaging agents are mainly inorganic nanomaterials, such as various noble-metal nanostructures,[4−12] carbon nanomaterials (e.g., carbon nanotubes and nanographene),[13−21] and copper-based nanoparticles.[22−25]

Compared with inorganic nanomaterials, organic nanomaterials are less frequently reported, and only limited types of these nanoparticles that are composed entirely of organic materials have been recently studied as potential contrast agents for in vivo PAT.[26−32] However, further studies on identifying more species of efficient photoacoustic contrast agents are restricted by the limited availability of NIR-absorbing polymers or dyes.[33] NIR-absorbing organic materials generally possess complicated π-conjugated systems that create difficulties during material design and synthesis. Thus, the fabrication of NIR-absorbing organic nanoparticles from simple materials is an attractive prospect for in vivo PAT.

Visible-light-absorbing squaraine dyes (SQs) are easily synthesized, have excellent photophysical properties,[34] and can be used for fluorescence imaging.[35−39] In aqueous solutions, SQs show a strong tendency to aggregate, resulting in red-shifted absorption from the visible to the NIR region. The resulting shift to NIR absorption benefits their potential application as PAT contrast agents in vivo. However, the resulting SQ aggregates cannot be used directly as biomaterials because they do not stably disperse in aqueous solution.[40] To address this issue, a novel NIR-absorbing organic nanoparticle based on SQ was successfully fabricated in this study by introducing albumin as the

Received: July 22, 2014
Accepted: September 16, 2014
Published: September 16, 2014

   dx.doi.org/10.1021/am504816h | ACS Appl. Mater. Interfaces 2014, 6, 17985−17992

protective carrier. This organic nanoparticle not only maintains the red-shift-induced NIR absorption of the SQ aggregate but also can stably disperse in aqueous solution with the albumin carrier (Scheme 1). The SQ we chose features a simple molecular

Scheme 1. Diagram of SQ Nanocomplex Preparation

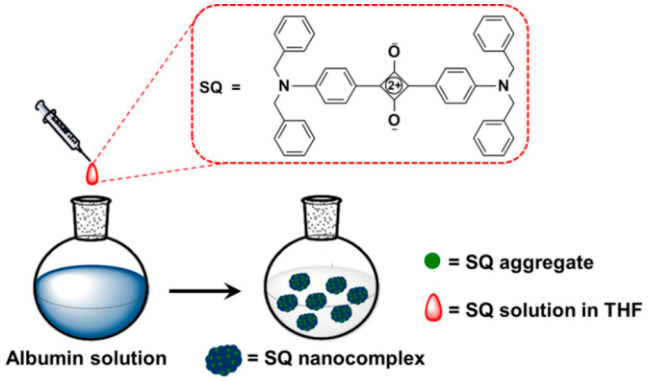

structure, single-step synthesis, high yield, and an absorption peak located within the visible-wavelength region (632 nm).[34] Upon nanocomplex formation, the hydrophobic SQ aggregates and disperses in water through albumin, which has been widely regarded as a highly biocompatible carrier.[41−43] The absorption spectrum of the aggregated SQ significantly widened up to the NIR region. The enhanced absorption in the NIR region made the SQ nanocomplex a more effective PAT contrast agent for in vivo liver and tumor imaging by reducing the noise signals originating from the vasculature.

MATERIALS AND METHODS

Materials. SQ was synthesized according to the literature.[34] Bovine serum albumin was purchased from Suzhou Alpha Biotech Co., Ltd. Tetrahydrofuran (THF) was purchased from Sigma-Aldrich Co., LLC.

Dynamic light scattering (DLS) was utilized to characterize the nanocomplex sizes in the aqueous solution (Malvern Instruments, Malvern, U.K.). Transmission electron microscopy (TEM) images were obtained using a Tecnai G2 F20 S-Twin transmission electron microscope (FEI Co., Hillsboro, OR). UV−vis−NIR spectra were obtained using a Lambda 750 UV−vis−NIR spectrophotometer (PerkinElmer, Waltham, MA).

Preparation of SQ Nanocomplexes. First, 500 mg of bovine serum albumin was dissolved in 100 mL of deionized water. Afterward, 30 mL of a solution of SQ in THF (0.11 mg mL^{-1}) was added dropwise with magnetic stirring. After 30 min, THF was removed via rotary evaporation. The remaining solution was centrifuged at 8000 rpm for 10 min. The supernatant was collected and further concentrated through ultrafiltration. Finally, the obtained sample was stored at 4 °C until use.

Characterization of SQ Nanocomplexes. DLS was used for the size characterization of the SQ nanocomplex in aqueous solution (Malvern Instruments, Malvern, U.K.). TEM images were obtained using a Tecnai G2 F20 S-Twin transmission electron microscope (FEI Co., Hillsboro, OR). UV−vis−NIR spectra were obtained using a Lambda 750 UV−vis−NIR spectrophotometer (PerkinElmer, Waltham, MA).

The PAT signal intensity determination of the SQ nanocomplex solution and PAT of the subcutaneously injected SQ nanocomplex were performed using homemade PAT equipment (AR-PAM system; see the Supporting Information, Figure S1). Commercial PAT equipment (MOST invision 128, Cold Spring Harbor Laboratory, Cold Spring Harbor, NY) was used for in vivo liver and tumor photoacoustic imaging.

In Vitro Stability of Nanocomplexes. SQ nanocomplexes were dispersed in deionized water. The nanocomplex diameters were measured using DLS on days 0, 4, and 141, and the statistical distribution of the diameters was obtained.

The stability of the SQ nanocomplex against hydrolysis was investigated through changes in the optical density (OD). An SQ nanocomplex solution with an initial OD of ∼0.47 was stored in a centrifuge tube at 4 °C. The OD was subsequently measured on day 141.

PAT Signal Intensity Determination of SQ Nanocomplex Solution. First, SQ nanocomplex solutions with different concentrations were placed in soft polyethylene tubes. The samples were then tested using the homemade PAT system with a 740 nm pulse laser. The signal intensities of 51 samples were counted and averaged to obtain plots of the concentration versus signal intensity. The PAT signal intensities of the free SQ and the corresponding carrier concentrations of the SQ nanocomplex were also measured using the homemade PAT system with a 740 nm pulse laser under the same conditions. The PAT imaging effect of the SQ nanocomplex solution (0.5 mM) was also evaluated using the commercial PAT equipment by placing the solution in a phantom tube and then analyzing it under different excitation wavelengths (710, 740, 770, 800, and 830 nm). A water blank was used as the control.

PAT of Subcutaneously Injected SQ Nanocomplexes. Female Bal b/c mice were shaved 2 days prior to the experiments. For subcutaneous imaging, the mice were anesthetized through intraperitoneal injection of 140 μL of pentobarbital sodium (1%). After 10 min, 25 μL of a SQ nanocomplex solution (0.06 mM) was subcutaneously injected into the right lateral back of each Bal b/c mouse. Treated animals were imaged using the homemade PAT equipment (AR-PAM system) with laser excitation at different wavelengths (532, 700, 740, and 800 nm). During imaging, laser pulses (with a repetition rate of 10 Hz and a pulse width of ∼15 ns) were coupled into a fiber and then passed through a dark-field illumination path before reaching the skin. A focused ultrasonic transducer (NA, 0.4; center frequency, 20 MHz) was used to detect PAT signals. Mounted on a motorized translational stage, the imaging system ran a 1D scan with a step size of 60 μm to provide a B scan. The 2D maximum amplitude projections were obtained by digitally processing and combining all of the B scans.

Photoacoustic Imaging of Liver in Vivo. Female Bal b/c mice were shaved 2 days prior to the experiments. Untreated Bal b/c mice were used as the controls, and the mouse livers were imaged using the commercial PAT equipment with a pulse laser excitation of 740 nm. Afterward, 200 μL of a SQ nanocomplex solution (0.5 mM) was intravenously injected into the same mice. After 6 h, the livers of the treated mice were imaged using the commercial PAT equipment with the same parameter settings. For image processing, the brightness bars of both images were set at the same scale so that the PAT effects could easily be compared.

Photoacoustic Imaging of Tumor in Vivo. Female Bal b/c mice were first shaved and then transplanted with 4T1 tumors. After 7 days, the mice were anesthetized through intraperitoneal injection of 140 μL of pentobarbital sodium (1%). After 10 min, the tumor-bearing mice were intratumorally injected with 100 μL of a SQ nanocomplex solution (0.5 mM) and imaged using the commercial PAT equipment. Tumor-bearing mice without SQ nanocomplex treatment were also imaged as the controls using the commercial PAT equipment.

Cytotoxicity Assessment of SQ Nanocomplex. 4T1 cells in 0.1 mL of the complete medium were seeded in 96-well plates (6000 cells $well^{-1}$) and incubated for 24 h. Afterward, 0.025 mL of a sterilized SQ nanocomplex solution with varying concentrations of phosphate-buffered saline (PBS) buffer was added to each well and incubated (37 °C, 5% CO_2). After 24 h, the medium was removed and each well was washed with PBS buffer twice. A total of 0.02 mL of a thiazolyl blue tetrazolium bromide solution (5 mg mL^{-1} in deionized water) was then added to each well. After 4 h, the solutions were removed and washed with PBS buffer twice. Next, 0.2 mL of dimethyl sulfoxide was added, and the plate was mixed for another 10 min. The relatively viable cells were finally quantified using a spectrophotometer by measuring the absorbance at 570 nm (ELISA reader). The cytoviabilities of the wells without added SQ nanocomplex were set as 1.0, while those of the others were calculated as relative values.

Blood Analysis and Histology Measurement. Nine healthy female Bal b/c mice were intravenously injected with a SQ nanocomplex solution (60 mg kg^{-1} per mouse) and sacrificed at 1, 7, and 19 days after injection (three mice per time point). Five Bal b/c mice were used as the controls. Blood was collected from the circulation of the treated mice for serum biochemistry assays and complete blood panel analysis, which were conducted by Shanghai Research Center for Biomodel Organism. Major organs from the treated mice were collected for hematoxylin and eosin (H&E) staining according to the standard protocol and examined using a digital microscope (Leica).

RESULTS AND DISCUSSION

The SQ nanocomplex was prepared by adding a solution of SQ in THF to albumin in deionized water under vigorous magnetic stirring (Scheme 1). Albumin has a solubility of 60 mg mL^{-1} in water but is insoluble in THF. Upon addition of the THF/SQ solution, the albumin solubility gradually decreased, resulting in aggregation into a non-cross-linked nanocomplex. The high hydrophobicity of SQ hinders its dispersion in water;[40] however, albumin acted as both a carrier and a dispersant and helped to disperse SQ in water. The diameters of SQ nanocomplex particles were measured using TEM, and most were found to be between 50 and 120 nm (Figure 1a). DLS analysis showed that

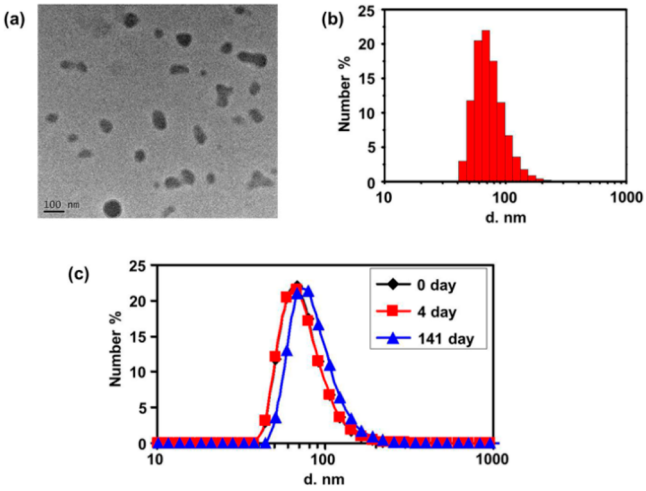

Figure 1. (a) TEM image of nanocomplexes. (b) Diameter distribution of nanocomplexes by DLS. (c) Diameter distribution of SQ–albumin nanocomplexes by DLS at days 0, 4, and 141.

the SQ nanocomplex particles have a diameter of ~76 nm with a polydispersity of 0.221 (Figure 1b). As a hydrophobic dye, SQ molecules aggregate and entangle with the hydrophobic domains of the albumin chains when added into an aqueous solution. The SQ molecules were trapped inside the nanocomplex during formation, thereby helping to disperse SQ in water. The SQ encapsulation efficiency was ~91%, and the drug loading was ~0.6%, as determined using chloroform extraction.

Glutaraldehyde is widely used as a cross-linker to prevent disassociation during the preparation of albumin nanospheres. However, the safety of glutaraldehyde is still controversial, and the clinical approval of glutaraldehyde-bearing materials for in vivo application has yet to be obtained.[44−46] Thus, the introduction of any cross-linker was avoided during preparation of the SQ nanocomplex. The nanocomplex is a noncovalent, supramolecular nanoaggregate of albumin and SQ. The ability of the nanocomplex to resist disassociation and maintain a stable diameter distribution was subsequently studied. The diameter of the nanocomplex remained almost unchanged after 4 days of storage, and the maximum particle size distribution was maintained at 76 nm. However, the polydispersity index (PDI) varied from 0.221 on day 1 to 0.194 on day 4 (Figure 1c), as characterized through DLS. After 141 days, the nanocomplex was again characterized using DLS, and the particle diameter was increased to 87 nm (PDI = 0.189). The stability of the nanocomplex was further investigated in PBS buffer. The result shows that the as-prepared nanocomplex exhibited relatively high stability during 2 days' tests (see the Supporting Information, Figure S2). The diameter slightly increased from 74 nm (PDI = 0.223) to 81 nm (PDI = 0.197).

In this study, SQ used was easily obtained at high yield through a single-step synthesis.[34] However, it exhibited a sharp absorption peak at 632 nm in THF (Figure 2a), which was

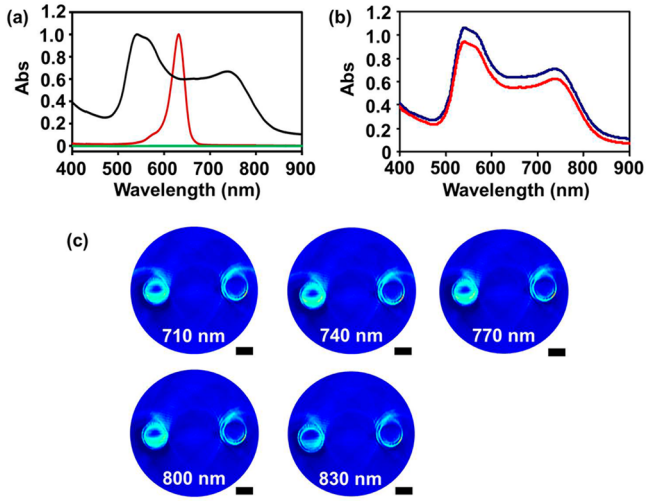

Figure 2. (a) Normalized absorption spectra of SQ in THF (red), SQ nanocomplexes in PBS buffer (black), and PBS buffer (green). (b) OD of SQ–albumin nanocomplexes at 0 days (blue) and 141 days (red). (c) PAT imaging effect of a SQ–albumin nanocomplex solution (0.5 mM, left) in phantom tubes compared to that of controls (water blanks, right) under excitation by different lasers (710, 740, 770, 800, and 830 nm). The scale bars in part c are all 3 mm.

located in the visible spectral region known to feature limited penetration depths in biological tissues with a PAT excitation light source.[2] In addition, biological tissues and components strongly absorb visible light and may generate strong PAT background noise under the excitation wavelengths used for PAT. This drawback may induce strong background signals and result in a suboptimal signal-to-noise ratio that would limit the effective application of SQ in PAT. Water-insoluble SQ has been previously reported to aggregate in aqueous solution.[39] During aggregation, the SQ absorption peak significantly widens up to the NIR region. In the present study, the SQ absorption peak was sharp and located at 632 nm in THF. However, its absorption was extended up to the NIR-wavelength region with the addition of water (see the Supporting Information, Figure S3). The widened absorption spectrum generally indicated the formation of SQ aggregates. The aggregation-induced variation of the absorption spectrum has been well studied previously, and it has been widely recognized that there are generally two types of aggregates for SQs: blue-shifted H-type aggregate in a pattern of head-to-head and red-shifted J-type aggregate in a pattern of head-to-tail.[47−49] The widened absorption spectrum of SQ

aggregates exhibited two typical absorption peaks around 532 and 740 nm. The SQ dye tended to form both H- and J-type aggregates, which showed blue-shifted and red-shifted absorption peaks, respectively. The J-type aggregation-induced NIR absorption is especially useful for preparing noninvasive PAT contrast agents because biological tissues are relatively transparent in the NIR region and the excitation laser can penetrate much deeper. Similarly, the as-prepared SQ nanocomplex also showed typical aggregation-induced NIR absorption in water (Figure 2a), which indicated the existence of SQ aggregates inside the SQ nanocomplex. The absorption peak of the SQ nanocomplex was also wide, spanning from the green region to the NIR region, which means that it can be used with a range of laser devices, not just with devices that generate a specific wavelength. The SQ nanocomplex showed robust stability against hydrolysis, as demonstrated by the OD variation. Figure 2b shows the OD of the SQ nanocomplex measured at 0 and 141 days. The OD was maintained at over 88% even after 141 days. The relatively stable OD not only implied that most SQ nanocomplex samples maintained excellent dispersion in aqueous solution but also demonstrated that the SQ nanocomplex is resistant to hydrolysis, thus allowing long-term storage. Because of the wide absorption peak of the SQ nanocomplex, the SQ nanocomplex solution can generate PAT signals under NIR excitation with wavelengths of 710, 740, 770, 800, and 830 nm (Figure 2c). The PAT signals generated by pulse lasers at 710, 740, 770, and 800 nm were stronger than that generated by the 830 nm laser. This result was consistent with the decreased light-absorption ability of the SQ nanocomplex in the wavelength region beyond 800 nm.

To understand the advantages of the aggregation-induced red shift for in vivo PAT application, 25 μL of a SQ nanocomplex solution was subcutaneously injected into the right lateral back of Bal b/c mice. The mice were then imaged using PAT equipment with different laser excitation wavelengths at 532, 700, 740, and 800 nm. Figure 3a shows that, at a laser excitation wavelength of

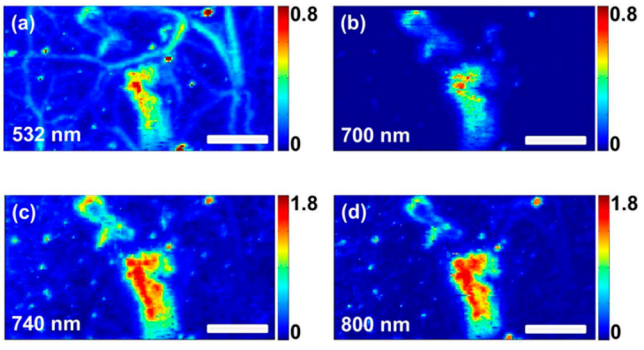

Figure 3. PAT of subcutaneous injection under excitation by different lasers: (a) 532 nm; (b) 700 nm; (c) 740 nm; (d) 800 nm. Scale bar = 2 mm.

532 nm, the vasculature was evidently visible against the injected PAT contrast agent. The signal from the vasculature was hardly noticeable under excitation by a 710 nm laser; however, the signal intensity of the injected PAT contrast agent was identical with that observed under 532 nm excitation light (Figure 3b). Similarly, under excitations of 740 and 800 nm, the signal intensity of the injected PAT contrast agent was strong, while the signal from the vasculature was significantly weakened and hardly noticeable (Figure 3c,d). The strong signal from the vasculature can be ascribed to the hemoglobin in blood, which can strongly absorb visible light and generate a PAT signal.[1] Blood components have relatively low absorption in the NIR region. Thus, the vascular signals in Figure 3c,d were significantly weakened, such that they hardly interfere with the signals from the PAT contrast agents. The weak signal of the vasculature under excitation by the NIR laser facilitated the reduction of background noise from the tissue itself, which will help to prevent false diagnosis. As a comparison, the mouse that was not injected with the PAT contrast agent was also imaged under excitation of lasers with different wavelengths (532, 700, 740, and 800 nm). As is shown in Figure S4 in the Supporting Information, the vascular signal is strong enough to be observed under excitation of a 532 nm laser but is invisible under excitation at NIR wavelengths. The results further demonstrate the advantage of the PAT contrast agent of an NIR-absorbing feature.

A 740 nm pulse laser was selected as the excitation light source to evaluate the SQ nanocomplex for subsequent biological applications because of its excellent imaging effect. SQ nanocomplex solutions with different concentrations were excited by a 740 nm pulse laser. After signal processing, the concentration was plotted versus the signal intensity and a good linear relationship was observed (R^2 = 0.9948; Figure 4). The

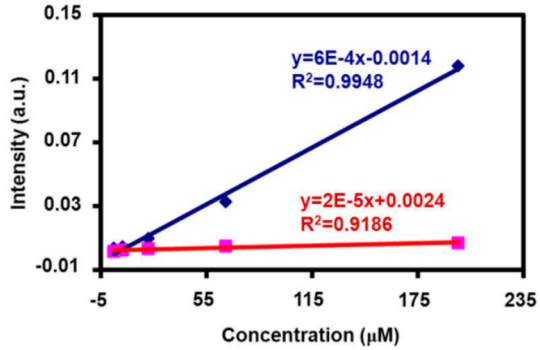

Figure 4. PAT signal intensities of a SQ–albumin nanocomplex (blue) and a free SQ solution (red) at different concentrations. Values are expressed as means ± standard deviation (n = 3).

intensity of the background noise was only 0.00151, which demonstrated that the as-prepared PAT contrast agent can be detected at concentrations as low as 2.4 μM. Compared with the SQ nanocomplex, the free SQ exhibited a sharp absorption peak at 632 nm, and its absorption in the NIR region decreased, making the signal significantly weaker. Correspondingly, the signal of the free SQ excited with a 740 nm laser showed almost no PAT signal (Figure 4). The PAT signal intensities of the corresponding SQ nanocomplex carrier concentrations were also negligible (see the Supporting Information, Figure S5). The results demonstrated that the strong PAT signal of the SQ nanocomplex was attributable to the aggregation-induced NIR absorption of the SQ dye in the nanocomplex.

The in vivo PAT application of the SQ nanocomplex was further evaluated by imaging the liver of a living mouse. Parts a and b of Figures 5 show that the signal from the liver before injection of the PAT contrast agent was weaker than that after injection. The enhanced PAT effect afforded by the SQ nanocomplex demonstrates that it can be used as a PAT contrast agent in the in vivo imaging of deep tissues and organs. For PAT imaging, a pulse laser is generally used, and the power of the laser must be restricted to avoid possible damage to the biological tissues and organs. PAT images of the livers were obtained prior

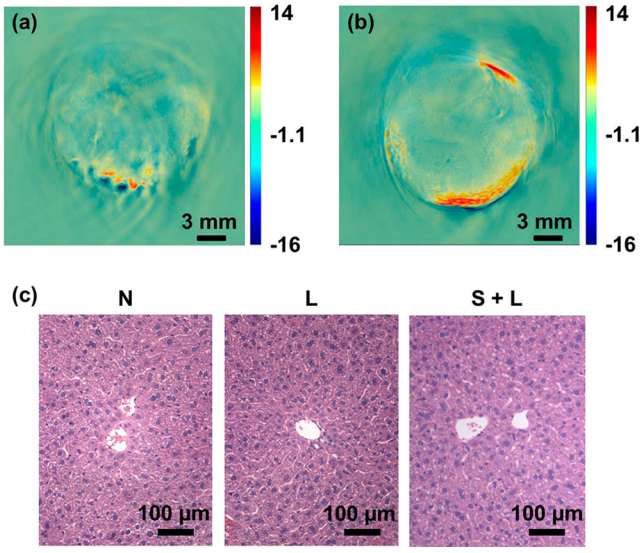

Figure 5. In vivo PAT images of liver (a) prior to and (b) 6 h after intravenous injection with a SQ–albumin nanocomplex (excitation wavelength = 740 nm). (c) Liver section from an untreated mouse (N), liver section from a liver control mouse (L), and liver section from a liver photoacoustic-imaging-treated mouse, which had been intravenously injected with a SQ–albumin nanocomplex 6 h before photoacoustic imaging (S + L).

to and after pulse irradiation, and the livers were then histologically examined through H&E staining of tissue sections. Hardly any damage was observed in the liver tissue after PAT imaging compared with the untreated liver tissue (Figure 5c). In addition, the SQ nanocomplex injection did not affect the safety of PAT in the liver (Figure 5c).

The SQ nanocomplex was further utilized in vivo as a 4T1 tumor contrast agent. The PAT imaging signal from the tumor of the untreated mouse was not distinguishable from that of the surrounding tissue (Figure 6a). In contrast, the signal from the

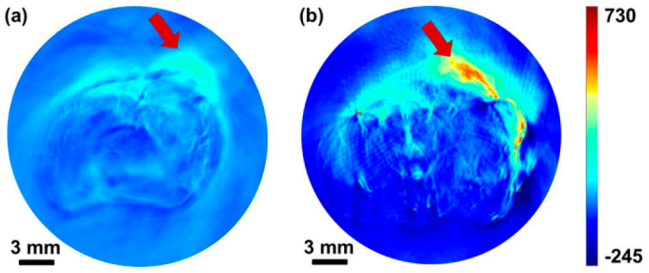

Figure 6. In vivo PAT images of tumor (a) without and (b) with SQ–albumin-nanocomplex injection. The arrows indicate tumors. Excitation wavelength = 740 nm.

tumor of the mouse that was injected with the SQ nanocomplex was evidently distinguishable from the surrounding normal tissue (Figure 6b). The significant contrast was ascribed to the stronger NIR-light absorption of the SQ nanocomplex compared with that of the tumor tissues in the untreated mouse and with healthy tissues and organs.

The cytotoxicity of the SQ nanocomplex against 4T1 cells was evaluated using a standard 3-(4,5-dimethylthiazol-2-yl)-2,5-diphenyltetrazolium bromide (MTT) assay. The results demonstrated that the nanocomplex had a slight influence on the viability of the 4T1 cells up to a concentration of 120 μM (see the Supporting Information, Figure S6). The biocompatibility of the SQ nanocomplex in living mice was evaluated through histological examinations on days 1, 7, and 19 after intravenous injection with the SQ nanocomplex solution. H&E-stained tissue sections of the liver, lung, spleen, and kidneys from the SQ-nanocomplex-treated groups showed no significant morphological difference compared with the untreated groups (Figure 7).

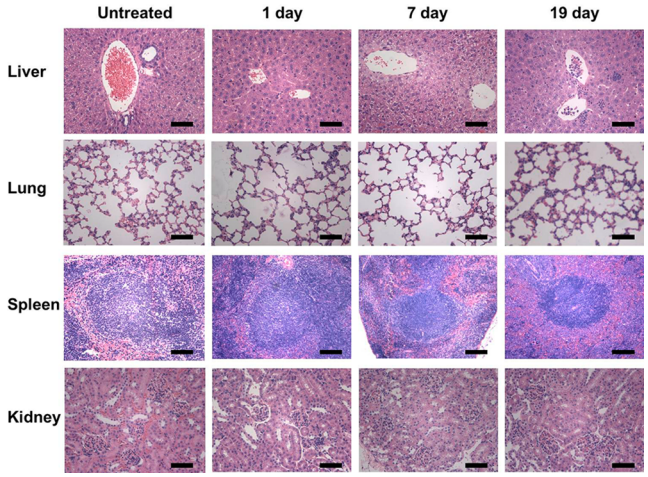

Figure 7. Sections of major organ slices from untreated mice and SQ–albumin-nanocomplex-treated mice 1, 7, and 19 days after intravenous injection. All of the scale bars are 100 μm.

Serum biochemical analysis was further performed on the mice on days 1, 7, and 19 after intravenous injection with the SQ nanocomplex solution. The liver is generally one of the main pathways for nanoparticle elimination and thus undertakes a significant physiological burden. Figure 8 shows that liver function parameters, including alanine aminotransferase (ALT), total protein (TP), and aspartate aminotransferase (AST), were generally normal and there was no evident hepatic toxicity. The TP level on day 1 was slightly lower than the normal reference range, but this minor difference was not statistically significant compared with the untreated controls. The kidney, another main route for nanoparticle elimination, is also placed under a physiological burden. Kidney function parameters, including blood urea nitrogen levels (BUN) and creatinine (CRE), showed no obvious indication of kidney toxicity (Figure 8). The BUN level on day 19 was slightly lower than normal, but compared with the data from the untreated animals, this difference was not statistically significant.

Blood panel assays were also performed on mice on days 1, 7, and 19 after intravenous injection of the SQ nanocomplex solution. During hematology analysis, the red blood cell count, hemoglobin levels, mean corpuscular volume, mean corpuscular hemoglobin, mean corpuscular hemoglobin concentration, and hematocrit levels were determined. All parameters in the treated groups appeared normal compared with those of the control group except for the mean corpuscular volume on days 7 and 19 and the hematocrit counts at day 7 after intravenous injection of a SQ nanocomplex solution (Figure 9). However, these minor differences were not statistically significant compared with the untreated controls. Although the systematic long-term toxicology of the SQ nanocomplex in mice requires further investigation, our preliminary results indicated that the SQ nanocomplex is not evidently toxic to mice.

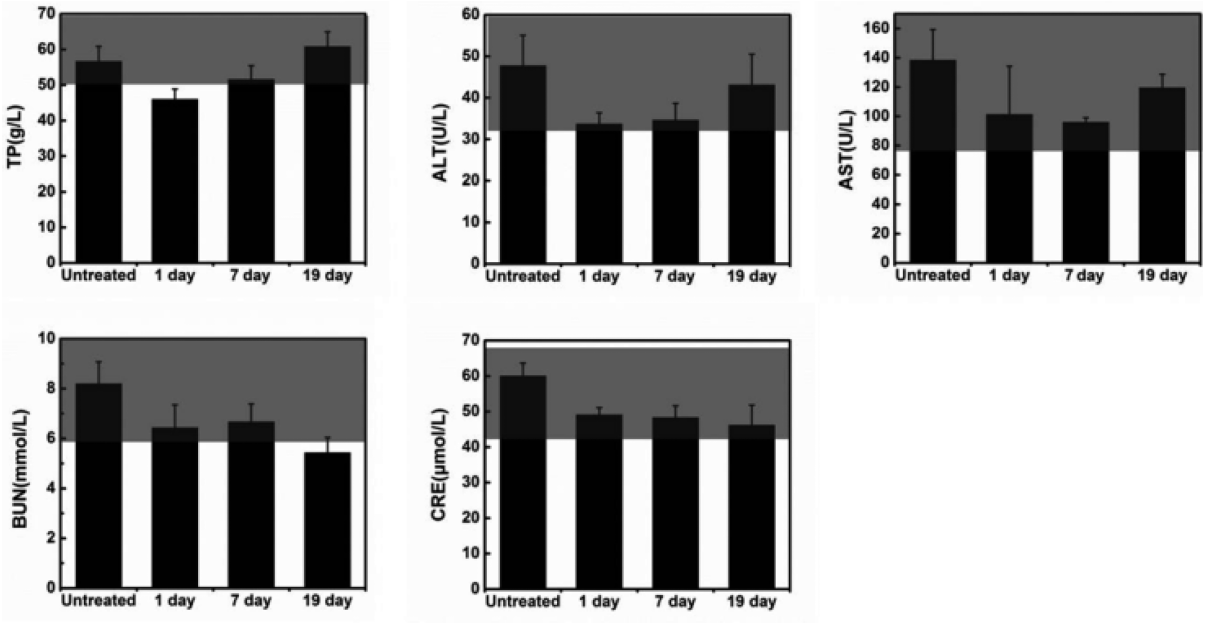

Figure 8. Serum biochemistry analysis of female Bal b/c mice treated with a SQ–albumin nanocomplex at a dose of 60 mg kg^{-1} at 1, 7, and 19 days after intravenous injection. Age-matched untreated mice were used as controls. Serum biochemistry data revealed that intravenous injection of the SQ–albumin nanocomplex did not induce any significant liver or kidney dysfunction, except with TP levels at day 1 and BUN levels at day 19, which were minor and not significantly different from those in the untreated control group. Gray areas show the normal reference ranges of hematology data for healthy female Bal b/c mice.

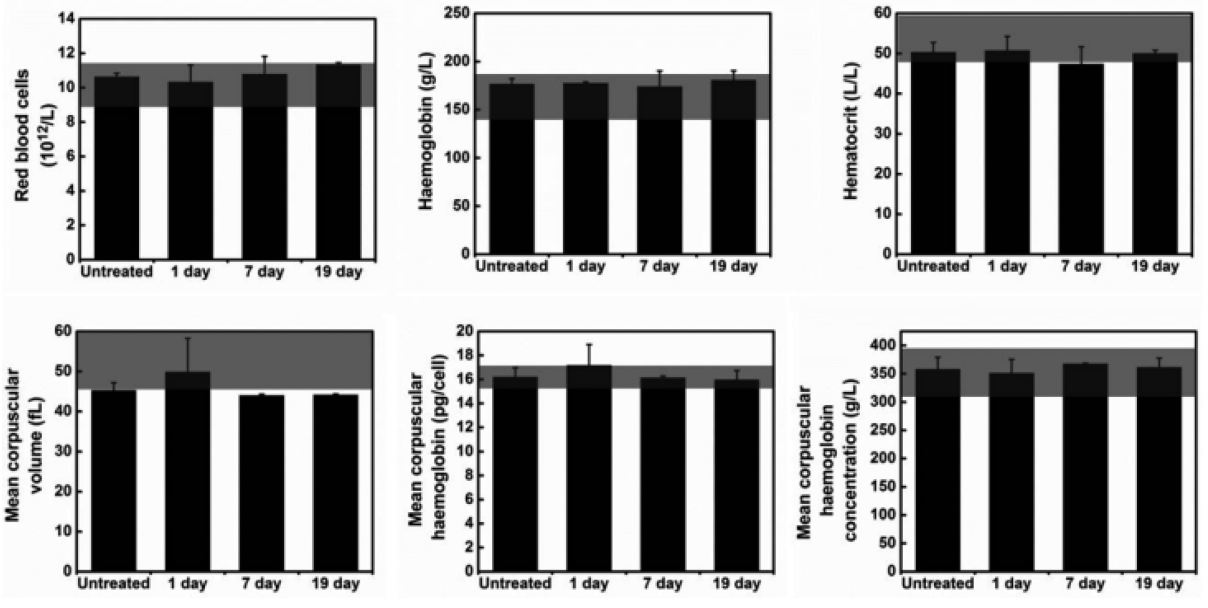

Figure 9. Blood panel data from healthy control and treated mice. The majority of the blood analysis data remained within normal ranges except the mean corpuscular volume on days 7 and 19 and the hematocrit counts on day 7, which were minor and not significantly different from those of the untreated control group. Error bars are based on three mice per group. Gray areas show normal reference ranges of hematology data for healthy female Bal b/c mice.

CONCLUSIONS

We developed an effective NIR PAT contrast agent by loading an aggregation-induced NIR-absorbing SQ dye into a water-dispersed albumin nanocomplex. The PAT contrast agent showed strong signals under a wide range of excitation wavelengths. Using green laser excitation in vivo, the vasculature gave strong background noise, but at NIR wavelengths, there was minimal background noise from the vasculature, and the NIR PAT contrast agent was successfully used for effective liver and tumor photoacoustic imaging. The SQ–albumin nanocomplexes showed good biocompatibility, inflicting only slight damage to the major organs, as well as having minor effects on the livers, kidneys, and physiological indices of living mice.

ASSOCIATED CONTENT

Supporting Information

Structure of the homemade PAT instrument, absorption spectrum of SQ aggregates in a mixed solution, PA signal

intensity of the carrier in SQ nanocomplexes, and MTT assay results of SQ–albumin nanocomplexes on 4T1 cells. This material is available free of charge via the Internet at http://pubs.acs.org.

AUTHOR INFORMATION

Corresponding Authors

*E-mail: chli@pku.edu.cn.

*E-mail: xhzhang@mail.ipc.ac.cn.

Author Contributions

‡These authors contributed equally.

Notes

The authors declare no competing financial interest.

ACKNOWLEDGMENTS

This work was supported by National Natural Science Foundation of China (Grants 91027021, 81171455, 61078073, and 31225009) and the National Basic Research Program of China (973 Program and Grants 2013CB933500, 2011CB808400, 2012CB932400, and 2011CB707502).

REFERENCES

(1) Wang, L. V.; Hu, S. Photoacoustic Tomography: In Vivo Imaging from Organelles to Organs. *Science* **2012**, *335*, 1458–1462.

(2) Pansare, V. J.; Hejazi, S.; Faenza, W. J.; Prud'homme, R. K. Review of Long-Wavelength Optical and NIR Imaging Materials: Contrast Agents, Fluorophores, and Multifunctional Nano Carriers. *Chem. Mater.* **2012**, *24*, 812–827.

(3) Kim, C.; Favazza, C.; Wang, L. V. In vivo Photoacoustic Tomography of Chemicals: High-Resolution Functional and Molecular Optical Imaging at New Depths. *Chem. Rev.* **2010**, *110*, 2756–2782.

(4) Kircher, M. F.; de la Zerda, A.; Jokerst, J. V.; Zavaleta, C. L.; Kempen, P. J.; Mittra, E.; Pitter, K.; Huang, R.; Campos, C.; Habte, F.; Sinclair, R.; Brennan, C. W.; Mellinghoff, I. K.; Holland, E. C.; Gambhir, S. S. A Brain Tumor Molecular Imaging Strategy Using a New Triple-Modality MRI-Photoacoustic-Raman Nanoparticle. *Nat. Med.* **2012**, *18*, 829–834.

(5) Wang, S.; Huang, P.; Nie, L.; Xing, R.; Liu, D.; Wang, Z.; Lin, J.; Chen, S.; Niu, G.; Lu, G.; Chen, X. Single Continuous Wave Laser Induced Photodynamic/Plasmonic Photothermal Therapy Using Photosensitizer-Functionalized Gold Nanostars. *Adv. Mater.* **2013**, *25*, 3055–3061.

(6) Liu, X.; Lee, C.; Law, W.-C.; Zhu, D.; Liu, M.; Jeon, M.; Kim, J.; Prasad, P. N.; Kim, C.; Swihart, M. T. Au–Cu_{2-x}Se Heterodimer Nanoparticles with Broad Localized Surface Plasmon Resonance as Contrast Agents for Deep Tissue Imaging. *Nano Lett.* **2013**, *13*, 4333–4339.

(7) Yang, H.-W.; Liu, H.-L.; Li, M.-L.; Hsi, I. W.; Fan, C.-T.; Huang, C.-Y.; Lu, Y.-J.; Hua, M.-Y.; Chou, H.-Y.; Liaw, J.-W.; Ma, C.-C. M.; Wei, K.-C. Magnetic Gold-Nanorod/PNIPAAmMA Nanoparticles for Dual Magnetic Resonance and Photoacoustic Imaging and Targeted Photothermal Therapy. *Biomaterials* **2013**, *34*, 5651–5660.

(8) Wilson, K.; Homan, K.; Emelianov, S. Biomedical Photoacoustics beyond Thermal Expansion Using Triggered Nanodroplet Vaporization for Contrast-Enhanced Imaging. *Nat. Commun.* **2012**, *3*, 618.

(9) Chen, Y.-S.; Frey, W.; Kim, S.; Kruizinga, P.; Homan, K.; Emelianov, S. Silica-Coated Gold Nanorods as Photoacoustic Signal Nanoamplifiers. *Nano Lett.* **2011**, *11*, 348–354.

(10) Jokerst, J. V.; Thangaraj, M.; Kempen, P. J.; Sinclair, R.; Gambhir, S. S. Photoacoustic Imaging of Mesenchymal Stem Cells in Living Mice via Silica-Coated Gold Nanorods. *ACS Nano* **2012**, *6*, 5920–5930.

(11) Homan, K. A.; Souza, M.; Truby, R.; Luke, G. P.; Green, C.; Vreeland, E.; Emelianov, S. Silver Nanoplate Contrast Agents for in vivo Molecular Photoacoustic Imaging. *ACS Nano* **2011**, *6*, 641–650.

(12) Nie, L.; Chen, M.; Sun, X.; Rong, P.; Zheng, N.; Chen, X. Palladium Nanosheets as Highly Stable and Effective Contrast Agents for In Vivo Photoacoustic Molecular Imaging. *Nanoscale* **2014**, *6*, 1271–1276.

(13) de la Zerda, A.; Liu, Z.; Bodapati, S.; Teed, R.; Vaithilingam, S.; Khuri-Yakub, B. T.; Chen, X.; Dai, H.; Gambhir, S. S. Ultrahigh Sensitivity Carbon Nanotube Agents for Photoacoustic Molecular Imaging in Living Mice. *Nano Lett.* **2010**, *10*, 2168–2172.

(14) Yang, K.; Hu, L.; Ma, X.; Ye, S.; Cheng, L.; Shi, X.; Li, C.; Li, Y.; Liu, Z. Multimodal Imaging Guided Photothermal Therapy Using Functionalized Grapheme Nanosheets Anchored with Magnetic Nanoparticles. *Adv. Mater.* **2012**, *24*, 1868–1872.

(15) Wang, C.; Ma, X.; Ye, S.; Cheng, L.; Yang, K.; Guo, L.; Li, C.; Li, Y.; Liu, Z. Protamine Functionalized Single-Walled Carbon Nanotubes for Stem Cell Labeling and In Vivo Raman/Magnetic Resonance/Photoacoustic Triple-Modal Imaging. *Adv. Funct. Mater.* **2012**, *22*, 2363–2375.

(16) Wang, Y.-W.; Fu, Y.-Y.; Peng, Q.; Guo, S.-S.; Liu, G.; Li, J.; Yang, H.-H.; Chen, G.-N. Dye-Enhanced Graphene Oxide for Photothermal Therapy and Photoacoustic Imaging. *J. Mater. Chem. B* **2013**, *1*, 5762–5767.

(17) Wu, L.; Cai, X.; Nelson, K.; Xing, W.; Xia, J.; Zhang, R.; Stacy, A.; Luderer, M.; Lanza, G.; Wang, L.; Shen, B.; Pan, D. A Green Synthesis of Carbon Nanoparticles from Honey and Their Use in Real-Time Photoacoustic Imaging. *Nano Res.* **2013**, *6*, 312–325.

(18) De La Zerda, A.; Zavaleta, C.; Keren, S.; Vaithilingam, S.; Bodapati, S.; Liu, Z.; Levi, J.; Smith, B. R.; Ma, T.-J.; Oralkan, O.; Cheng, Z.; Chen, X.; Dai, H.; Khuri-Yakub, B. T.; Gambhir, S. S. Carbon Nanotubes as Photoacoustic Molecular Imaging Agents in Living Mice. *Nat. Nanotechnol.* **2008**, *3*, 557–562.

(19) Kim, J.-W.; Galanzha, E. I.; Shashkov, E. V.; Moon, H.-M.; Zharov, V. P. Golden Carbon Nanotubes as Multimodal Photoacoustic and Photothermal High-Contrast Molecular Agents. *Nat. Nanotechnol.* **2009**, *4*, 688–694.

(20) de la Zerda, A.; Bodapati, S.; Teed, R.; May, S. Y.; Tabakman, S. M.; Liu, Z.; Khuri-Yakub, B. T.; Chen, X.; Dai, H.; Gambhir, S. S. Family of Enhanced Photoacoustic Imaging Agents for High-Sensitivity and Multiplexing Studies in Living Mice. *ACS Nano* **2012**, *6*, 4694–4701.

(21) Yu, J.; Yang, C.; Li, J.; Ding, Y.; Zhang, L.; Yousaf, M. Z.; Lin, J.; Pang, R.; Wei, L.; Xu, L.; Sheng, F.; Li, C.; Li, G.; Zhao, L.; Hou, Y. Multifunctional Fe_5C_2 Nanoparticles: A Targeted Theranostic Platform for Magnetic Resonance Imaging and Photoacoustic Tomography-Guided Photothermal Therapy. *Adv. Mater.* **2014**, *26*, 4114–4120.

(22) Ku, G.; Zhou, M.; Song, S.; Huang, Q.; Hazle, J.; Li, C. Copper Sulfide Nanoparticles as a New Class of Photoacoustic Contrast Agent for Deep Tissue Imaging at 1064 nm. *ACS Nano* **2012**, *6*, 7489–7496.

(23) Pan, D.; Cai, X.; Yalaz, C.; Senpan, A.; Omanakuttan, K.; Wickline, S. A.; Wang, L. V.; Lanza, G. M. Photoacoustic Sentinel Lymph Node Imaging with Self-Assembled Copper Neodecanoate Nanoparticles. *ACS Nano* **2012**, *6*, 1260–1267.

(24) Zha, Z.; Zhang, S.; Deng, Z.; Li, Y.; Li, C.; Dai, Z. Enzyme-Responsive Copper Sulphide Nanoparticles for Combined Photoacoustic Imaging, Tumor-Selective Chemotherapy and Photothermal Therapy. *Chem. Commun.* **2013**, *49*, 3455–3457.

(25) Liu, X.; Law, W.-C.; Jeon, M.; Wang, X.; Liu, M.; Kim, C.; Prasad, P. N.; Swihart, M. T. Cu_{2-x}Se Nanocrystals with Localized Surface Plasmon Resonance as Sensitive Contrast Agents for In Vivo Photoacoustic Imaging: Demonstration of Sentinel Lymph Node Mapping. *Adv. Healthcare Mater.* **2013**, *2*, 952–957.

(26) Filonov, G. S.; Krumholz, A.; Xia, J.; Yao, J.; Wang, L. V.; Verkhusha, V. V. Deep-Tissue Photoacoustic Tomography of a Genetically Encoded Near-Infrared Fluorescent Probe. *Angew. Chem., Int. Ed.* **2012**, *51*, 1448–1451.

(27) Huynh, E.; Lovell, J. F.; Helfield, B. L.; Jeon, M.; Kim, C.; Goertz, D. E.; Wilson, B. C.; Zheng, G. Porphyrin Shell Microbubbles with Intrinsic Ultrasound and Photoacoustic Properties. *J. Am. Chem. Soc.* **2012**, *134*, 16464–16467.

(28) Zha, Z.; Deng, Z.; Li, Y.; Li, C.; Wang, J.; Wang, S.; Qu, E.; Dai, Z. Biocompatible Polypyrrole Nanoparticles as a Novel Organic Photoacoustic Contrast Agent for Deep Tissue Imaging. *Nanoscale* **2013**, *5*, 4462–4467.

(29) Ayala, L. Virus-Mimicking Nano-constructs as a Contrast Agent for Near Infrared Photoacoustic Imaging. *Nanoscale* **2013**, *5*, 1772−1776.
(30) Guo, M.; Mao, H.; Li, Y.; Zhu, A.; He, H.; Yang, H.; Wang, Y.; Tian, X.; Ge, C.; Peng, Q.; Wang, X.; Yang, X.; Chen, X.; Liu, G.; Chen, H. Dual Imaging-Guided Photothermal/Photodynamic Therapy Using Micelles. *Biomaterials* **2014**, *35*, 4656−4666.
(31) Pu, K.; Shuhendler, A. J.; Jokerst, J. V.; Mei, J.; Gambhir, S. S.; Bao, Z.; Rao, J. Semiconducting Polymer Nanoparticles as Photoacoustic Molecular Imaging Probes in Living Mice. *Nat. Nanotechnol.* **2014**, *9*, 233−239.
(32) Huynh, E.; Jin, C. S.; Wilson, B. C.; Zheng, G. Aggregate Enhanced Trimodal Porphyrin Shell Microbubbles for Ultrasound, Photoacoustic, and Fluorescence Imaging. *Bioconjugate Chem.* **2014**, *25*, 796−801.
(33) Escobedo, J. O.; Rusin, O.; Lim, S.; Strongin, R. M. NIR Dyes for Bioimaging Applications. *Curr. Opin. Chem. Biol.* **2010**, *14*, 64−70.
(34) Arunkumar, E.; Forbes, C. C.; Noll, B. C.; Smith, B. D. Squaraine-Derived Rotaxanes: Sterically Protected Fluorescent Near-IR Dyes. *J. Am. Chem. Soc.* **2005**, *127*, 3288−3289.
(35) Jisha, V. S.; Arun, K. T.; Hariharan, M.; Ramaiah, D. Site-Selective Binding and Dual Mode Recognition of Serum Albumin by a Squaraine Dye. *J. Am. Chem. Soc.* **2006**, *128*, 6024−6025.
(36) Jisha, V. S.; Arun, K. T.; Hariharan, M.; Ramaiah, D. Site-Selective Interactions: Squaraine Dye−Serum Albumin Complexes with Enhanced Fluorescence and Triplet Yields. *J. Phys. Chem. B* **2010**, *114*, 5912−5919.
(37) Zhang, Y.; Yue, X.; Kim, B.; Yao, S.; Bondar, M. V.; Belfield, K. D. Bovine Serum Albumin Nanoparticles with Fluorogenic Near-IR-Emitting Squaraine Dyes. *ACS Appl. Mater. Interfaces* **2013**, *5*, 8710−8717.
(38) Gao, F.-P.; Lin, Y.-X.; Li, L.-L.; Liu, Y.; Mayerhöffer, U.; Spenst, P.; Su, J.-G.; Li, J.-Y.; Würthner, F.; Wang, H. Supramolecular Adducts of Squaraine and Protein for Noninvasive Tumor Imaging and Photothermal Therapy In Vivo. *Biomaterials* **2014**, *35*, 1004−1014.
(39) Xu, Y.; Li, Z.; Malkovskiy, A.; Sun, S.; Pang, Y. Aggregation Control of Squaraines and Their Use as Near-Infrared Fluorescent Sensors for Protein. *J. Phys. Chem. B* **2010**, *114*, 8574−8580.
(40) Zhang, C.; Zhang, X.; Zhang, X.; Fan, X.; Jie, J.; Chang, J. C.; Lee, C.-S.; Zhang, W.; Lee, S.-T. Facile One-Step Growth and Patterning of Aligned Squaraine Nanowires via Evaporation-Induced Self-Assembly. *Adv. Mater.* **2008**, *20*, 1716−1720.
(41) Elsadek, B.; Kratz, F. Impact of Albumin on Drug Delivery—New Applications on the Horizon. *J. Controlled Release* **2012**, *157*, 4−28.
(42) Elzoghby, A. O.; Samy, W. M.; Elgindy, N. A. Albumin-Based Nanoparticles as Potential Controlled Release Drug Delivery Systems. *J. Controlled Release* **2012**, *157*, 168−182.
(43) Kratz, F.; Elsadek, B. Clinical Impact of Serum Proteins on Drug Delivery. *J. Controlled Release* **2012**, *161*, 429−445.
(44) Sung, H. W.; Huang, D. M.; Chang, W. H.; Huang, L. L. H.; Tsai, C. C.; Liang, I. L. Gelatin-Derived Bioadhesives for Closing Skin Wounds: An In Vivo Study. *J. Biomater. Sci. Polym. Ed.* **1999**, *10*, 751−771.
(45) Liu, B. S.; Yao, C. H.; Hsu, S. H.; Yeh, T. S.; Chen, Y. S.; Kao, S. T. A Novel Use of Genipin-Fixed Gelatin as Extracellular Matrix for Peripheral Nerve Regeneration. *J. Biomater. Appl.* **2004**, *19*, 21−34.
(46) An, F. F.; Yang, Y. L.; Liu, J.; Ye, J.; Zhang, J. F.; Zhou, M. J.; Zhang, X. J.; Zheng, C. J.; Liang, X. J.; Zhang, X. H. A Reticuloendothelial System−Stealthy Dye−Albumin Nanocomplex as a Highly Biocompatible and Highly Luminescent Nanoprobe for Targeted In Vivo Tumor Imaging. *RSC Adv.* **2014**, *4*, 6120−6126.
(47) Yan, Z.; Xu, H.; Guang, S.; Zhao, X.; Fan, W.; Liu, X. Y. A Convenient Organic−Inorganic Hybrid Approach Toward Highly Stable Squaraine Dyes with Reduced H-Aggregation. *Adv. Funct. Mater.* **2012**, *22*, 345−352.
(48) Chen, H.; Law, K.-Y.; Perlstein, J.; Whitten, D. G. Amphiphilic Squaraine Dye Aggregates: Evidence for a Cyclic Chiral Structure as a General Supramolecular Structure for Aggregates of Dyes and Aromatic Molecules. *J. Am. Chem. Soc.* **1995**, *117*, 7257−7258.
(49) Alex, S.; Basheer, M. C.; Arun, K. T.; Ramaiah, D.; Das, S. Aggregation Properties of Heavy Atom Substituted Squaraine Dyes: Evidence for the Formation of J-Type Dimer Aggregates in Aprotic Solvents. *J. Phys. Chem. A* **2007**, *111*, 3226−3230.